Deep super-resolution imaging of thick tissue using structured illumination with adaptive optics

Jingyu Wang[1,2,*], Danail Stoychev[1,2,*], Mick Phillips[1], David Miguel Susano Pinto[1,2], Richard M. Parton[1], Nick Hall[1], Josh Titlow[1], Ana Rita Faria[1], Matthew Wincott[2], Dalia Gala[1], Andreas Gerondopoulos[1], Niloufer Irani[1], Ian Dobbie[1,3,#], Lothar Schermelleh[1,#], Martin Booth[2,#], Ilan Davis[1,#]

[1] Department of Biochemistry, University of Oxford, South Parks Road, Oxford OX1 3QU, UK
[2] Department of Engineering, University of Oxford, Parks Road, Oxford OX1 3PJ, UK
[3] Current address: Department of Biology, Johns Hopkins University, Baltimore, MD-21218, USA
* Contributed equally to the work
[#] Correspondence: ilan.davis@bioch.ox.ac.uk, martin.booth@eng.ox.ac.uk, ian.dobbie@jhu.edu, lothar.schermelleh@bioch.ox.ac.uk

Abstract

3D structured illumination microscopy (3D-SIM) doubles the resolution of fluorescence imaging in lateral and axial directions and increases contrast in both fixed and live specimens. However, 3D-SIM has so far not been widely applied to imaging deep in thick tissues due to its sensitivity to specimen-induced aberrations, making the method difficult to apply beyond 10 µm in depth. Furthermore, 3D-SIM has not been available in an upright configuration, limiting its use for live imaging while manipulating the specimen, for example with electrophysiology. Here, we have overcome these barriers by developing a novel upright 3D-SIM system (termed Deep3DSIM) that incorporates adaptive optics (AO) for aberration correction and remote focusing, reducing artefacts, and removing the need to move the specimen or objective. Both these advantages are equally applicable to inverted 3D-SIM microscopes. We demonstrate high-quality 3D-SIM imaging up to 130 µm into complex tissue and live sample manipulation, including human cells and *Drosophila* larval brains and embryos.

Keywords

Super-resolution microscopy (SRM), 3D structured illumination microscopy (3D-SIM), aberration correction, deep imaging, adaptive optics (AO), deformable mirror (DM), remote focusing, spatial light modulator (SLM), neuroscience, nervous system, electrophysiology, *Drosophila*, live cell imaging

Introduction

Fluorescence microscopy has greatly advanced with the development of super-resolution microscopy techniques that enable biological imaging with spatial resolutions well below the optical diffraction limit (Huang et al., 2009; Sahl et al., 2017; Schermelleh et al., 2019; Schermelleh et al., 2010). One of these approaches is 3D structured Illumination microscopy (3D-SIM) which features two-fold increased resolution in each spatial direction and enables fast optical sectioning with strongly enhanced imaging contrast. This approach recovers missing high spatial frequency information by illuminating the specimen with finely patterned illumination across the specimen and computational reconstruction (Gustafsson et al., 2008; Schermelleh et al., 2008). 3D-SIM has become increasingly popular amongst cell biologists, as it is compatible with standard fluorophores and labelling protocols commonly used in widefield or confocal microscopy.

Over the past decade, several off-the-shelf 3D-SIM instruments have become commercially available and have been successfully used for various biological applications. However, all share certain limitations that restrict their usage to thin specimens on inverted setups. Optical aberrations are a main contributor to common reconstruction artefacts in 3D-SIM imaging (Demmerle et al., 2017). These include (1) spherical aberration induced by refractive index (RI) mismatches between the immersion media, mounting media, and sample, and (2) sample-induced aberrations caused by RI inhomogeneities within the specimen. As their deteriorating effects increase with imaging depth, it is currently difficult to obtain artefact-free 3D-SIM images at a depth greater than around 10 µm and over larger z-ranges in most specimens when using high numerical aperture (NA) oil-immersion objectives. Effective imaging depth may be increased to some extent using silicon-immersion objectives, which are designed for use with an immersion fluid with an RI closer to that of tissue, thus reducing spherical aberration. Currently, no upright, off-the-shelf SIM microscope systems exist that use water-dipping objectives, e.g. to carry out live neuroscience experiments with electrophysiology or other workflows involving imaging without a coverslip and providing access to the specimen and its manipulation while imaging. There are two reasons for this limitation. First, water-dipping objectives are more sensitive to aberrations than, for example, silicon immersion objectives due to RI mismatch and movement induced by living specimens. Second, the optical pathways of upright microscopes present technical challenges to the accommodation of 3D-SIM functionality, together with the ergonomic constraints required to allow access to the specimen for manipulation. Due to its rigid requirement of an optimal point spread function (PSF), 3D-SIM requires high mechanical stability, which potentially conflicts with the need for specimen manipulation for neuroscience experiments that require a large working distance and involve movement of the sample platform or instrument. Therefore, the benefits of 3D-SIM have not

been utilised in large areas of biology such as, for example, live cell imaging of nervous system preparations while manipulating the specimen.

An obvious solution to the above limitation is to incorporate adaptive optics (AO) using a deformable mirror (DM) in the optical path of a 3D-SIM microscope. AO would not only enable the correction of spherical and specimen-induced aberrations, but it would also allow remote focusing without the need to move the specimen or objective. These functionalities have been described as prototype methods for widefield (Kam et al., 2007), and 3D-SIM (Lin et al., 2021; Thomas et al., 2015; Turcotte et al., 2019; Žurauskas et al., 2019) as well as for remote focusing for multiphoton imaging (Žurauskas et al., 2017). However, none of the off-the-shelf 3D-SIM instruments are designed to allow the inclusion of AO. Moreover, AO hardware and software controls are currently not available as simple modules that can be added to the optical path of commercial systems. While some exciting bespoke-built AO-SIM systems have previously been described (Li et al., 2017; Lin et al., 2021; Thomas et al., 2015; Turcotte et al., 2019), these proof-of-principle prototypes use AO for aberration correction only and are not suitable for general biological applications and certainly not for applications requiring an upright optical configuration with multiple channels. To our knowledge, DM-driven remote focusing, although well studied in both simulation (Kner et al., 2011) and experiments, for example, in confocal (Poland et al., 2008) and multiphoton imaging, has not been implemented on any 3D-SIM systems.

Here, we describe our bespoke upright 3D-SIM prototype microscope system with integrated AO, enabling deep imaging in live wholemount biological specimens with access to manipulating the specimen (**Fig. 1**). The system is based around a 60x/1.1 NA water-dipping objective for which we demonstrate high-quality 3D-SIM with nearly two-fold spatial resolution extension in three dimensions at depths from a few µm up to 130 µm deep. We use AO not only for sample-induced aberration correction in deep tissue imaging but also for remote focusing, which enables fast transitions of the imaging plane and prevents pressure waves caused by the motion along the optical axis of the specimen or the objective lens. Our novel approach and instrument design enables simultaneous multichannel imaging in conventional and super-resolution modes, with acquisitions of fast Z-stacks and timelapse, deep in live specimens while keeping them accessible to experimental manipulation. The modular design and user-friendly open-source Python software of Deep3DSIM (see Methods and Materials) allow for convenient sample navigation and a simple workflow for routine biological experiments. We first verify the system performance using beads and cells in culture. We then apply the full range of novel imaging modalities available on Deep3DSIM to a wide range of specimen types, from mammalian tissue culture cells to *Drosophila* larval brains and embryos. Finally, although our use of AO for aberration correction and remote focusing is demonstrated on an upright microscope with water-dipping objectives, the

principles we have established could be applied equally to an inverted 3D-SIM system to extend the depth of imaging considerably and to allow more rapid acquisition of 3D stacks without the need to move the specimen or the objective.

Results

To initially assess the baseline performance of Deep3DSIM in applications where there are minimal aberrations, we imaged 100 nm diameter green-fluorescent beads. We used 3D images of beads to estimate the PSF in all imaging modalities (**Fig. 2A, B**). We first compared the performance in widefield in two configurations – standard microscope optics without AO correction by using a DM-bypass (BP) optical path (labelled as BP WF) and then with AO correction for system aberrations (labelled as AO WF). We expected minimal aberrations to affect images of beads mounted under a coverslip following careful adjustment of the collar of the objective designed for correcting spherical aberration. Correspondingly, we found that in the widefield (WF) mode, using AO to correct system aberrations led to a small improvement in the overall shape of the PSF compared with the standard WF using BP. This improvement was evident when measuring the full width at half maximum (FWHM) of the PSF in the X and Z direction, which changed from 286 nm and 970 nm, respectively, in BP WF to 281 nm and 901 nm in AO WF (**Fig. 2A, B**). Next, we acquired equivalent results using the DM to change the microscope's plane of focus, which we refer to as remote focusing (RF) and compared these measurements to those from conventional acquisition of a z-stack with a piezo Z stage. Widefield RF imaging results in PSFs with an FWHM resolution that is very close to that using AO system correction or DM-bypass, namely 282 nm and 848 nm respectively (**Fig. 2A, B** as RF WF). When acquiring images of the same beads using 3D-SIM with AO (AO SIM), we measured an FWHM of 176 nm laterally and 566 nm axially, equivalent to an ~5-fold volumetric resolution improvement over uncorrected BP WF. It is worth noting that the resolution improvement is close to but not quite reaching the expected half of the calculated widefield diffraction limit in each axis, that is, 281 nm (in XY) and 851 nm (in Z) for the 1.1 NA of the water-dipping objective used. One reason for this is that we opted for a conservative linewidth of the structured illumination pattern to be 310 nm, which is larger than the theoretical optimal value of 285 nm to prevent accidental clipping on the DM (see Supplementary Information for details).

3D-SIM, like other super-resolution methods, is sensitive to low levels of system and specimen-induced aberrations, even at a depth typical of single cells in culture. Such minor aberrations tend to be insignificant in conventional microscopy modalities such as widefield and confocal (Wang and Zhang, 2021). Therefore, we first verified the degree of resolution enhancement by 3D-SIM in mammalian tissue culture COS-7 cells (**Fig. 2C**, left) with microtubules immunofluorescently labelled using Alexa Fluor (AF) 488 conjugated antibodies

and, in another example, endoplasmic reticulum labelled with antibodies against Rtn4 and conjugated to AF555 (**Fig. 2C**, right). Compared to the corresponding widefield images, the optical sectioning capability of 3D-SIM is easily noticeable by the large difference in out-of-focus signal in **Fig. 2C**, especially in the XZ cross-section view displayed below the XY views. The resolution enhancement can also be confirmed in the Fourier space as shown in **Fig. 2D**, where the widefield power spectrum is mostly concentrated in the central area, the SIM data presents a much more even distribution across the frequency space, extended to the high-frequency region beyond 200 nm. Because of the high spatial information carried by the microtubule structures, a radial integration of the 2D power spectrum provides a close estimation of the system OTF where lateral resolution can be measured; they were measured by the position of the inflection point (arrowheads) to be 330 nm and 187 nm, respectively for widefield and SIM modes, close to the FWHM values measured from beads data shown in **Fig. 2A**. The performance of the system in the red channel is similar except for a slight reduction of frequency range due to the longer wavelength. Here, the resolutions measured from the Fourier power plots in widefield mode and 3D-SIM mode are 403 nm and 208 nm, respectively.

A significant benefit and uniqueness of the Deep3DSIM design is its upright configuration, whereas commercial SIM systems are built around inverted microscopes and are usually restricted to imaging thin samples, such as cultured cells. The Deep3DSIM system is therefore applicable to tissue-based imaging and live experiments such as electrophysiology. We evaluated the applicability of these unique capabilities of the instrument to thick biological specimens that have a substantial degree of RI inhomogeneity, leading to optical aberrations. We used AO SIM to image the thick and complex tissues of fixed *Drosophila* larval neuromuscular junction (NMJ) preparation. We imaged larvae from a transgenic line expressing a bright GFP protein trap of the cell-cell “septate” junction protein Neurexin IV (Nrx-IV), at a depth of 5-15 μm (**Fig. 3**). The images of the AO-corrected volume showed significant improvements in both intensity and contrast after reconstruction, compared with images of the uncorrected volume (**Fig. 3**). The improvement was especially noticeable between the XZ views in **Fig. 3A, B**, as the major effect of aberrations is to distort the PSF along the optical axis. This is particularly the case for the dominant spherical aberration, which elongates the focus along the optical axis but is also an effect of other aberration modes, such as coma, which typically lead to a bending of the PSF in cross-section view.

To further test the microscope’s performance at greater depth, we imaged dissected and subsequently formaldehyde-fixed whole *Drosophila* larval brains. We imaged both the top and bottom layers of the thickest part of the brain lobes, mounted between a standard microscope coverslip (#1.5) and a slide, providing a total imaging depth of up to ~130 μm

185 (**Fig. 4C**). To help visualise the effects of aberrations and evaluate the ability of AO to correct them at depth, we placed 100 nm diameter red fluorescent beads (580/605 nm) on the glass slide underneath the tissue. We imaged two 4-5 µm thick image stacks centred around two sites – one ~3 µm and another ~130 µm away from the cover slip – which required focusing through the entire volume of the mounted brain (**Fig. 4**). We found that AO
190 aberration correction made a small but noticeable improvement to the contrast on the proximal side of the brain lobe (**Fig. 4A**). On the distal side, control images bypassing the AO suffered from severe aberration-induced reconstruction artifacts, with the cell membranes not being observable as continuous structures (**Fig. 4B**, left). In contrast, imaging at the same depth with AO correction enabled 3D-SIM reconstructions to produce
195 clearer 3D images with reduced artefacts and enhanced contrast. Large areas of the cell membranes could be visualised showing the expected overall structure (**Fig. 4B**, right). The effect of aberrations and their correction is impressively clear in the red channel, where the signal of individual beads closely mimics the shape of the system PSF while the equivalent image without AO presents large, unrecognizable pseudo-structures. The aberration
200 correction method employed here effectively estimated a correction averaged across the entire FOV of 68 x 68 µm at 130 µm depth. It is worth noting that aberrations can differ across larger fields, and therefore, after applying an average correction, residual aberrations can still be observed in some regions of the AO-corrected bead images. However, the overall PSF shapes were still dramatically improved with AO compared to the equivalent
205 without AO. Finally, the peak intensity and SNR with AO are significantly higher than the results without AO, as shown in the example intensity profile plots in **Fig. 4D**.

Biological samples, even adherent cells in culture, can be thick enough to induce substantial aberrations which vary considerably throughout the volume of a specimen. Therefore, effective correction needs to be modified at different depth levels, while acquiring
210 extended image stacks. As the Deep3DSIM system is capable of rapidly changing the focal position through remote focusing, we demonstrated combined remote focusing with AO aberration correction on cells in culture (**Fig. 5**). In principle, it would be possible to perform aberration measurements at every imaging plane within the volume. However, such an approach requires a disproportionate measurement time before each acquisition, which
215 might lead to unnecessary photobleaching and phototoxicity. As we found that the aberrations change approximately linearly in depth, we could measure the aberration in two planes and calculate the corrections in intermediate planes by interpolation, an approach which we termed “multi-position AO”. To test multi-position AO, we imaged fixed COS-7 cells in culture stained for microtubules, to visualise the spindles during mitosis. We measured the
220 aberrations at the top and the bottom of the cells, and then applied an interpolated correction at different Z positions between the two measured planes. Our results show conclusively that

remote focusing with aberration correction produced images with improved contrast and resolution compared to remote focusing without aberration correction. The improvements provided by interpolated aberration corrections were particularly noticeable in point-like structures in the specimens (**Fig. 5A**, right). In contrast, such points result in elongated structures when imaged without aberration correction (**Fig. 5A**, left). **Fig. 5B** displays the image intensity of two line profiles in X and Z directions without and with multi-position AO for comparison, demonstrating increased signal intensity with AO correction, in addition to the resolution improvement. In the case of the X profile plot (**Fig. 5B**, top), although two peaks can be separated without AO, indicated by the red arrows, the distance is enlarged compared to that in the image with AO due to the aberration-induced distortion of the sample structure (**Fig. 5A**, insets).

One of the challenges of 3D-SIM has been its limited ability to carry out live cell imaging rapidly and in thick specimens (Gao et al., 2012). Living specimens are particularly challenging for two reasons. First, the structures can change within the time it takes to acquire a 3D volume. Second, imaging through living material causes more pronounced aberrations compared with fixed material, in which the RI is increased and made more homogenous by introducing a mounting medium with high RI, such as glycerol. The Deep3DSIM approach has the potential to resolve both these challenges. Aberration correction can, in principle, be used to correct more severe aberrations. In addition, using our interpolation approach to calculate the shape of the mirror required for correction of aberrations, as opposed to simply measuring the shape, is much quicker, enabling faster SIM to match dynamic biology.

To test the feasibility of 3D-SIM for dynamic live biological imaging, we imaged *Drosophila* embryos undergoing rapid mitosis (**Fig. 6**). We collected eggs from transgenic animals expressing the microtubule-binding protein Jupiter fused to GFP and the histone H2A proteins fused to RFP. The Jupiter::GFP, H2A::RFP eggs were dechorionated and mounted in aqueous solution in order to image chromosomes and microtubules simultaneously, during mitotic division in the syncytial blastoderm stages of early *Drosophila* embryos. We used remote focusing to repeatedly acquire two-colour image volumes at a depth of 5 μm under the surface at a rate of 20 fps, equivalent to 10 s per 3D volume at room temperature for several minutes. Each image stack of 7 z-sections required 210 raw images (5 phases x 3 angles x 2 λ) for 3D-SIM reconstruction. Using AO-based aberration correction with interpolation, combined with remote focusing, we were able to obtain an effective time sequence of 3D-SIM stacks with reduced residual aberrations. **Fig. 6A** displays lateral mid-sections of five selected time points within the first two minutes of the time series, showing the synchronous transition from metaphase to telophase. Five different Z positions from one selected timepoint are displayed in **Fig. 6B**. These results demonstrate

that the remote focusing functionality of the system can be successfully applied for live 3D-SIM experiments, allowing four-dimensional acquisition while keeping the specimen stationary, thus avoiding the usual agitation and perturbations associated with mechanical actuation.

Discussion

We have demonstrated that the design of Deep3DSIM, a prototype upright super-resolution microscope with integrated AO, enables effective 3D super-resolution imaging within thick complex tissues to a depth of at least 130 µm. Its modular design and Python-based open-source software for both system control and GUI (see details in Methods and Materials), make it comparatively user-friendly and versatile. These design concepts allow the adaptation of the instrument to suit specific research applications and enable protocols for experiments at scale. The upright optical design combined with aberration correction and remote focusing renders the instrument particularly suited for applications that require super-resolution volumetric imaging of live (or fixed) thick tissue, organs, or whole organisms. Importantly, the design is compatible with specimen manipulation, such as microinjection, carrying out electrophysiology measurements, or adding reagents to specimens during imaging experiments. In this study, we have established a new paradigm for 3D-SIM to be applied at depth while acquiring volumes without moving the specimen or the objective and while varying the aberration corrections across the acquired volume, in a depth-specific manner. This general principle can now be applied to any SIM configuration, including an inverted one, which can make use of the highest possible NA objectives to obtain volumetric SIM datasets at depth with minimal artifacts and maximum possible spatial resolution.

Current commercially available 3D-SIM instruments are mostly based around inverted setups and high NA oil immersion objectives that are susceptible to aberrations when focusing into any specimens with RI mismatch, therefore frequently only producing good images up to depths of a few µm. When such instruments are used with silicon immersion objectives, with slightly reduced NA, high-quality SIM can be extended to a depth of around 20 µm (Ogushi et al., 2021; Richter et al., 2019). In all cases, objective correction collars can only effectively minimise spherical aberrations for SIM imaging in a single channel. For multi-colour imaging, the RI of the mounting medium and the immersion medium (or the objective's correction collar setting) have to be carefully fine-tuned to match to the recorded wavelength-specific OTFs and to find a suitable compromise to accommodate multiple colours (Demmerle et al., 2017; Wang et al., 2018). Therefore, for most practical purposes, these microscopes can only effectively be applied to thin single layers of tissue culture cells on microscope slides or only to the superficial surface of complex tissues that are relatively optically transparent. Furthermore, they are not readily

adapted to imaging regimes which require the specimen and the objective to remain motionless while imaging. Hence, Deep3DSIM fills an important application gap for deep imaging in live multi-cellular tissue. The method creates new possibilities for future biological investigations, such as super-resolution imaging in live specimens or whole animals, imaging fast live 3D time-lapse movies while carrying out specimen manipulations, for example micro-injection into *Drosophila* embryos, or carrying out electrophysiology measurements on living mouse brain sections or *Drosophila* NMJ preparations while imaging.

The range of remote focusing shown in this work was limited to ±5 µm, which is smaller than some previous demonstrations. There were two reasons for the choice of this range. First, the deformable mirror can only reliably produce PSFs with minimal aberration repeatedly in this range (see Supplementary Information). Second, for 3D-SIM acquisition, 10 µm is a commonly used Z range. Especially in multi-color imaging, a rather large number of images, about 1200 frames per channel, would be required. While larger volume acquisition is possible, it would lead to considerable photobleaching and phototoxicity, as well as longer acquisition and reconstruction times. Moreover, there is a trade-off between the number of volumes that can be acquired (number of time points) and the number of Z-sections within the volume.

The resolution achieved with Deep3DSIM was 176 nm FWHM at 488 nm using a water-dipping objective with an NA of 1.1. In comparison, inverted commercial 3D-SIM instruments routinely achieve 100-120 nm resolution at 488 nm using a high-NA oil immersion objective. While the Deep3DSIM resolution is therefore lower in absolute terms, this was a design trade-off chosen to make the microscope compatible with live imaging in an upright configuration and with a large working distance. Hence, it is more pertinent to compare the resolution of Deep3DSIM to that achievable for live cell imaging in widefield microscopy, using the same NA water-dipping objective, which is 286 nm in the green channel and 336 nm in the red channel. However, the fundamental design of the Deep3DSIM microscope could be readily adapted, if necessary, to work in upright or inverted mode with other objective lenses, including oil or silicone immersion objectives to achieve higher spatial resolution, while still benefitting from the use of AO for motionless deep imaging. In these cases, the working distance would be compromised, making it much more difficult to manipulate the sample, for example by microinjection or with electrophysiology tools. Nevertheless, the implementation of AO hardware and software described in this report is suitable for most widefield-based instruments, including SIM that would benefit from the incorporation of a DM if it can easily be added to the optical path. Although the design of Deep3DSIM was mostly optimised for upright microscopy with tissue specimens, it can also benefit other types of microscopy and applications. Notably, CryoSIM (Kounatidis et al., 2020) would hugely benefit from the inclusion of AO to correct for

spherical aberrations induced by increased RI mismatch at cryogenic temperatures together with sampled-induced aberration, particularly with non-flat overlying ice at the specimen-air interface.

There are various routes through which the system performance could be enhanced in future versions of Deep3DSIM. First, the speed of acquisition in the reported demonstration was limited by a few key system components, which could be improved in future developments. A key limiting factor in widefield mode was the EM-CCD camera. The best overall performance in terms of structured illumination modulation was achieved when using conventional CCD modes. However, due to the data transfer time (3 MHz pixel readout rate), the frame rate was limited to about 100 fps for a reasonable size field of view. This acquisition speed could be increased by using newer sCMOS cameras. In addition, in SIM experiments the imaging speed was also limited by the update rate of the spatial light modulator (SLM), determined by the settling time of the nematic liquid crystal technology (around 20-40 ms), giving a maximum frame rate of 50 fps raw data. Fast SLMs using ferroelectric liquid crystal materials have been demonstrated in SIM for high-speed SIM imaging (Lin et al., 2021), though it is more challenging to use such SLMs for multi-colour imaging, as the phase modulation is binary and hence optimised for a single wavelength. Third, future improvements could also include the incorporation of denoising algorithms into the reconstruction process to allow lower light dosage, which would enable faster imaging, reduced photobleaching, and reduced specimen photodamage. Combinations of such hardware and software improvements would enhance acquisition speed for realistic experimental situations, imaging live biological processes in super-resolution at high volumetric and temporal rates. Finally, in the future, the optical path of Deep3DSIM could be simplified and reduced in size, thus making it easier to adopt or commercialise, as well as building specific Deep3DSIM systems designed for bespoke applications.

Methods and materials

Microscope platform

We based the Deep3DSIM system on our previous bespoke Cryo-SIM setup (Phillips et al., 2020). The microscope body is built in an upright configuration (**Fig. 1**) and is designed around a water-dipping objective lens (Olympus LUMFLN60XW), which was selected for imaging of tissues, particularly for *Drosophila* brain, NMJ, and electrophysiological experiments. With the goal of flexibility and ease of use, especially to assist with fast and accurate sample navigation, we also included a low-magnification dry lens (Olympus LMPLFLN10X). The objective lenses were mounted at fixed positions, and the sample was translated in 3D by a set of X, Y, and Z stages. Images from the two objective lenses were

mapped in 3D so that the same sites could be revisited with minimal error by both objective lenses. The XY translation was handled by a large-opening motorised stage (PI M-687.UN) and the Z translation was handled by a combination of a heavy-duty linear stage (Aerotech PRO115) and piezo stage (PI P-736.ZCN) for accurate and fast motion during experiments. The microscope body was connected optically to the rest of the system with a periscope. More details about the optical setup can be found in the Supplementary Information.

Structured illumination

To implement 3D SIM, we adopted mid-speed analogue SLM (Boulder Nonlinear Systems, HSP512-488-800) to produce structured illumination. The SLM was positioned in the sample-conjugated plane and linear sinusoidal patterns were generated for three orientation angles. The ±1st order and zero-order beams were used to interfere at the sample plane to generate the 3D structured illumination. To achieve optimal interference contrast, the linear polarisation of the excitation beam from the SLM was rotated using a liquid crystal device (Meadowlarks Optics, LPR-100-λ) to maintain S polarisation at the incident plane at the back pupil of the objective lens for each SI orientation. For widefield acquisitions, the SLM was switched off and used as a single reflector so that only the zero-order beam provided epi-illumination; while for SIM acquisition, the SLM was switched on and it was preloaded with the SI patterns that were generated according to the wavelength and the line width specified by the user in the software before acquisition. During image acquisition, the SI phase and angle were rotated in a fixed sequence, synchronised with the polarisation rotators, the light sources, and the cameras.

Deformable mirror

Sensorless AO was chosen for the correction of aberration, as it is simple and effective to implement (Žurauskas et al., 2019). A deformable mirror (Alpao DM69-15) was positioned at the back-pupil conjugated plane, between the main dichroic filter and the microscope body, so that the DM was used for correcting both the excitation and emission paths. The DM aperture was matched to cover the back-pupil of the objective lens by relay. An integrated interferometer was used to calibrate the DM for both aberration correction and remote focusing (optical path illustrated in yellow dotted line in **Fig. S1**). A pair of flip mirrors were included to create an optical path that bypassed the DM (referred to as the “DM-bypass” path), to permit easy comparison between conventional imaging and that with AO aberration correction.

Software

The system control software package was composed of three parts (**Fig. 1C**): *python-microscope* for low-level hardware control of the entire optomechanical system (Susano Pinto et al., 2021), *microscope-cockpit* for a user interface and experiments (Phillips et al., 2022), and *microscope-aotools* for performing DM calibration and AO aberration correction (Hall et al., 2020). All three were further developed and improved, and links to the latest repositories can be found in the Supplementary Information. For SIM data reconstruction, we used a commercial package softWoRx (GE Healthcare). OTFs required for reconstruction for each imaging channel were generated from experimental data acquired from a single fluorescent bead. Multi-colour image alignments were performed in the open-source software Chromagnon (Matsuda et al., 2018). SIM characterization was done with SIMcheck (Ball et al., 2015). General image processing was done in Fiji (Schindelin et al., 2012).

Sensorless AO

Modal-based approaches for adaptive optics were used for wavefront control. The DM was calibrated to generate control metrics that delivered accurate wavefronts in Zernike modes (Antonello et al., 2020). An integrated interferometer was built into the optical path that could be folded into the microscope when required. A quality control based on Zernike modes was implemented in *microscope-aotools* and regularly used to verify the accuracy of the DM. A Fourier domain image metric was used for optimizing each Zernike mode, for specimens with structures of sufficiently high spatial frequency (Hall, 2020) . When the spatial frequencies were not high enough, ISOsense (Žurauskas et al., 2019) was adopted to achieve a more robust AO correction.

Multi-position aberration correction

We used multi-position aberration correction to compensate for the optical distortions in thick volumes. We applied our standard sensorless AO routine at fixed positions, e.g. at the top and the bottom of the volume, and then we fitted the resulting correction Zernike coefficients to a line, assuming the RI changed in a linear manner with Z within the chosen volume. This simplification allowed us to calculate in advance the corrections required at every section of the volume. All patterns necessary for an experiment were registered to Z location and queued on the DM device. TTL triggers were then used in real-time to cycle through the patterns, while updating imaging position either with the piezo Z stage or with the DM-driven remote focusing.

Remote focusing

Remote focusing is highly desired in neuronal imaging and other experiments, such as electrophysiology, where it is required that the sample remains stationary during acquisitions. AO can be used to replace piezo Z stage (Žurauskas et al., 2017). We controlled the remote focusing and the aberration correction independently, each one with its own set of corrections, which were then summed together if both functionalities were to be used simultaneously. To calculate the required remote focusing corrections, we first performed a calibration experiment where we used a sample with a single layer of fluorescent beads. The sample was displaced by the piezo Z stage first in one direction and then by the same amount in the opposite direction. Sensorless AO correction was used at both positions to correct for Zernike modes, which included defocus (Z4) and spherical aberrations (Z11, Z22, etc). We then performed a linear fit of the corrections and their corresponding Z positions, and we used this model as a look-up table to calculate the remote focusing pattern for all Z positions. This approach achieved a linear response with high precision on the Alpao DM69-15, within a range of 10 μm, but the accuracy was found lacking. This is not surprising to us, as this DM is known to have a creep effect (Bitenc et al., 2014). The dynamic characteristics of the device are discussed in more detail in the Supplementary Information. We found that in practice the response can vary by a scaling factor related to the speed with which the DM shape was varied. To determine this scaling factor, we established a second calibration step where the piezo Z stage was used as a reference to displace the sample of beads in Z and provide ground-truth values. While performing the scale calibration, we matched the displacements by the remote focusing that is interpolated from the linear fitting with the displacement by the piezo stage, taking measurements of multiple points along the Z range. We then performed a linear fitting of both the remote focusing and the piezo stage Z points, and we related the two slopes to derive the scaling factor. Similarly to multi-position AO correction, all remote focusing patterns were computed in advance before image acquisition. They were then added to the aberration correction patterns and the results were queued on the DM driver. During image acquisition, TTL triggers were used to cycle through all queued patterns and to synchronise with the rest of the hardware.

Cell culture

COS-7 (ATTC) cells were grown on #1.5 glass coverslips in DMEM containing 10% fetal bovine serum (Sigma-Aldrich), washed twice with 2 ml of 100 mM sodium phosphate and fixed for 2 h in 2 ml PLP (2% [wt/vol] paraformaldehyde in 87.5 mM lysine, 87.5 mM sodium phosphate pH 7.4 and 10 mM sodium periodate). Coverslips were washed three times in 2 ml (100 mM) sodium phosphate, pH 7.4, before permeabilization in 1 mg/ml BSA, 0.05%

480 saponin, and 100 mM sodium phosphate, pH 7.4, for 30 min. In all cases, primary antibody (α-Tubulin (mouse; DM1A Santa Cruz) AF488 and Rtn4 (rabbit; AbD Serotec) AF555) staining was performed in 1 mg/ml BSA, 0.05% saponin, and 100 mM sodium phosphate, pH 7.4 for 60 min at room temperature. Affinity-purified antibodies were used at 1 µg/ml; commercial antibodies were used as directed by the manufacturers. DAPI was added to the
485 secondary antibody staining solution at 0.3 µg/ml. Coverslips were mounted in Mowiol 4-88 mounting medium (EMD Millipore).

Fly strains

The following fly lines were used in this study. Nrx-IV::GFP (CA06597, kindly gifted by the
490 Rita Teodoro lab) for the NMJ samples, cno::YFP (CPTI000590, DGRC 115111) for the brain samples, Jupiter::GFP, his2A::RFP (Hailstone et al., 2020) for embryos. All stocks were raised on standard cornmeal-based medium at 25ºC.

Fixed Drosophila larval fillet for imaging of neuromuscular junctions

495 The NMJ samples were prepared by following the protocol in (Brent et al., 2009), apart from the fixation, which was done in 4% paraformaldehyde (PFA) in PBSTX (phosphate-buffered saline with 0.1% Triton X-100) for 30 min and then followed by two washes for 20 min each in PBSTX. The samples were then incubated with Cy3-conjugated α-HRP antibody (1:500, Jackson ImmunoResearch 123-165-021) for 1 h. Finally, the samples were washed in
500 PBSTX for 45 min and then mounted in Vectashield. All steps were done at room temperature.

Fixed whole Drosophila brains

Third instar *Drosophila* larvae were dissected in PBS. Brains were removed and fixed in 4%
505 PFA in PBSTX (0.3% Triton X-100) for 25 min. Afterwards, they were rinsed three times in PBSTX, further permeabilised with two 20 min washes, and then mounted in PBS.

Drosophila embryos for live imaging

The live embryo samples were prepared as described in (Parton et al., 2010), except that
510 they were mounted in PBS.

Acknowledgements

John Sedat for the original optical design, similar design is described in (Phillips et al., 2020); Antonia Göhler and Mantas Žurauskas for the initial optical characterization, work which was
515 published previously; Martin Hailstone, Francesca Robertson, and Jeff Lee for preparing

specimens during various phases of using the Deep3DSIM instruments with biology, imaging that was not shown in the manuscript. JW thanks Jacopo Antonello, Chao He and Jiahe Cui for insightful discussions and advice for AO devices. We are grateful to Micron Oxford and its numerous partners and staff for discussions and providing the environment required for the success of this complex interdisciplinary technology development project.

Funding

DSP, IMD, ID, MP, NH, and RMP were funded by Wellcome Trust (091911/Z/11/Z, 096144/Z/11/Z, 105605/Z/14/Z, 107457/Z/15/Z, 203141/Z/16/Z, 209412/Z/ 17/Z). JW, MW, and MB were funded by European Research Council (AdOMiS, No. 695140). The research was further supported by Medical Research Council grant [MR/K01577X/1] to ID. LS acknowledges support by the European Union's Horizon 2020 research and innovation program under the Marie Sklodowska-Curie Grant Agreement No. 766181. DS was funded by a BBSRC iCASE studentship to ID and MB sponsored by Aurox.

Author contributions

Original vision and concept development: ID, IMD, RMP
Designed the microscope optics: ID, IMD, MP
Designed and implemented the optomechanics: MP
Implemented electronics: DS, MP, IMD
Implemented initial optical system: IMD, NH, MP
Development of control software: DS, MP, IMD, DSP, NH, MW, JW
Developed adaptive optics methods, algorithms and calibration: NH, JW, DS, MB
Implemented remote focusing method: JW, DS
Acquisition of initial data: IMD, NH, JT, RMP
Refined and reimplemented optical system and adaptive optics control: JW, DS
Refined experimental processes: JW, DS, LS, RF, RMP
Experimental strategy and specimen preparation: JW, DS, LS, RP, RF, AG, NI, DG, RMP
Imaging experiments, calibration, and data processing: JW, DS, LS
Article conceptualisation: ID, LS, JW, DS, MB, RMP
Initial draft of article and figure preparation: ID, DS, JW
Revision of article: ID, LS, JW, DS, MB, IMD
Obtaining funding: ID, MB, LS
Supervision: IMD, ID, MB, LS

550 **Figures**

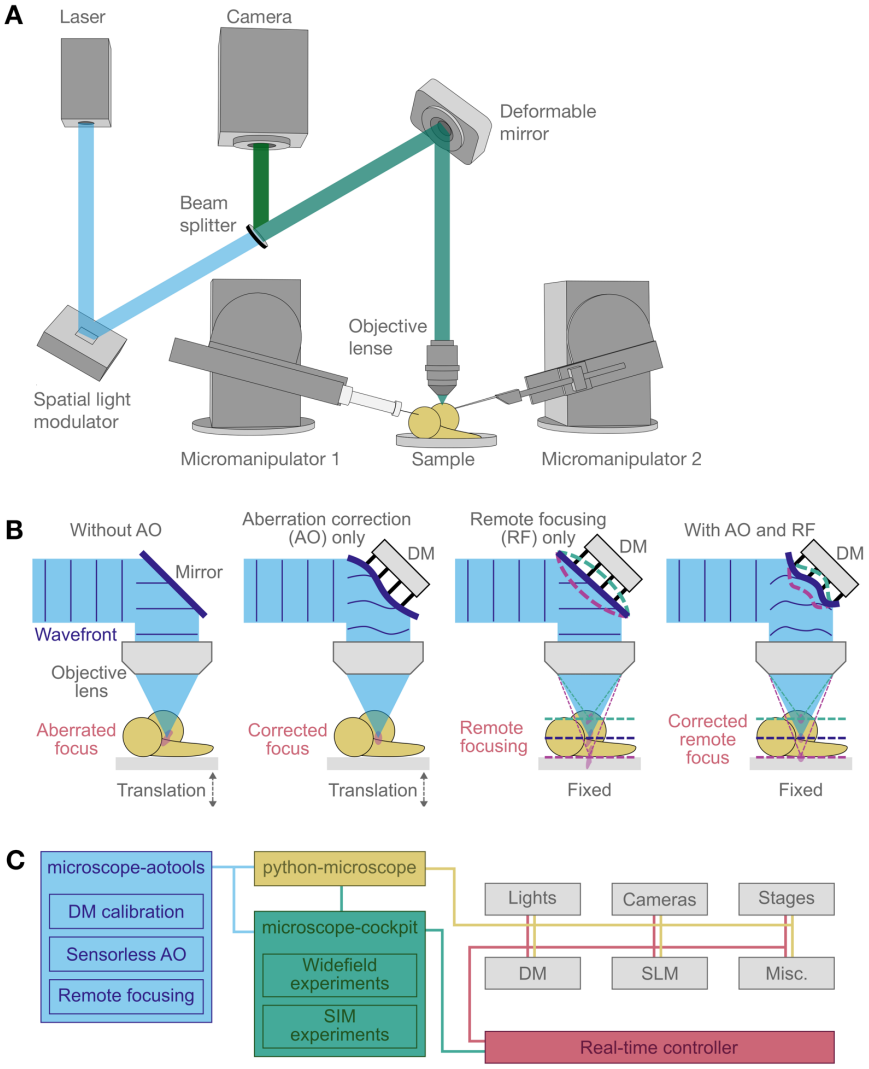

Figure 1. Simplified overview of the Deep3DSIM setup. (**A**) The optical arrangement shows the upright configuration of Deep3DSIM allowing the use of micromanipulators for
555 applications such as microinjection and electrophysiology. The excitation light is incident on a spatial light modulator (SLM), which is conjugated to the object/image plane, and then reflected off a deformable mirror (DM) before being focused on the sample with an objective lens. In the imaging path, the reflected fluorescence is coupled off via a dichroic beam splitter and then collected by separate cameras for each channel. (**B**) Different imaging
560 modes are enabled in parallel on Deep3DSIM. Deep imaging without AO usually leads to an aberrated PSF due to RI mismatch and sample inhomogeneity. Sensorless AO correction compensates for sample-induced aberrations. Remote focusing (RF) enables fast focusing at various depths without moving the specimen/objective. Coupling AO and RF produces aberration-corrected imaging at different depths, without mechanical movement. (**C**)

Deep3DSIM is controlled by Cockpit, which consists of 3 packages: python-microscope is responsible for the control of all hardware devices; microscope-cockpit provides a user-friendly GUI; microscope-aotools provides the AO functionality. The system uses a real-time controller, in this case, the Red Pitaya STEMlab 125-14, to coordinate different instruments for image acquisition with structured or widefield illumination.

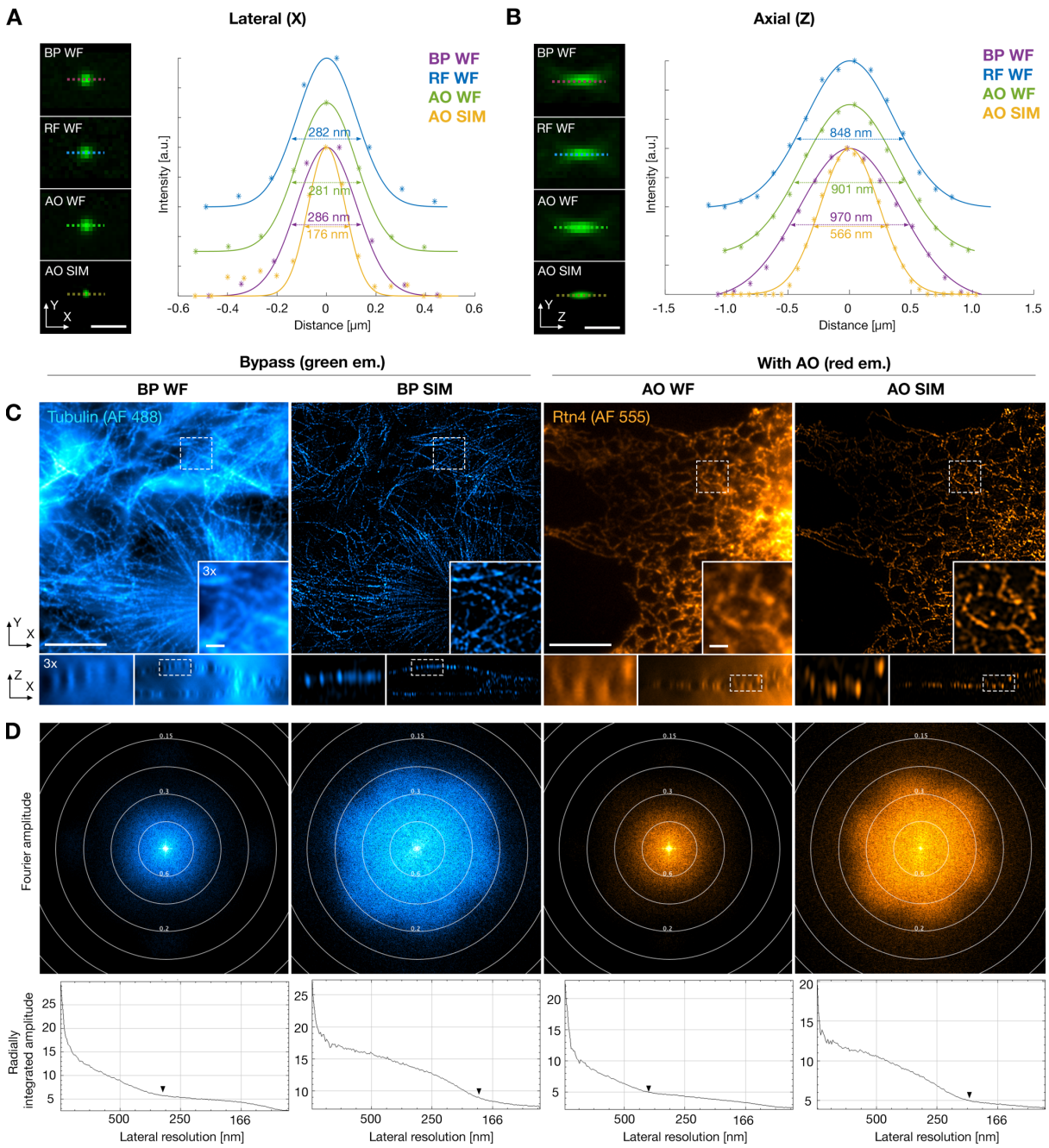

Figure 2. Characterization of the Deep3DSIM system. Lateral (**A**) and axial (**B**) PSF for the different modalities of the instrument measured from 100 nm green-fluorescent beads. Widefield DM-bypass (BP WF), widefield with AO (AO WF), widefield with aberration correction and remote focusing (RF WF), and 3D-SIM with AO (AO SIM). The images in XY plane and the XZ plane with a plot of the PSF at the peak in X and Z direction are displayed from left to right. Scale bar: 500 nm. (**C**) Widefield (WF) and 3D-SIM images acquired from COS-7 cells in XY and XZ view, which show AF488 antibody labeled microtubules acquired in the green channel (LUT cyan hot) and Rtn4 detected with AF555 antibody labeling the endoplasmic reticulum in the red channel (LUT orange hot); the dotted boxed areas in all

images are shown in 3x zoom in subsets. Scale bars: 10 μm and 1 μm (insets). (**D**) Corresponding Fourier amplitude in XY spatial frequency space, where spatial information enhancement due to SIM can be observed from the widefield data (left) to the SIM data (right) in green and red channels. Radially integrated amplitude of XY Fourier projection of widefield and SIM (right) are displayed underneath, where the highest achieved resolution is measured and indicated by black arrows.

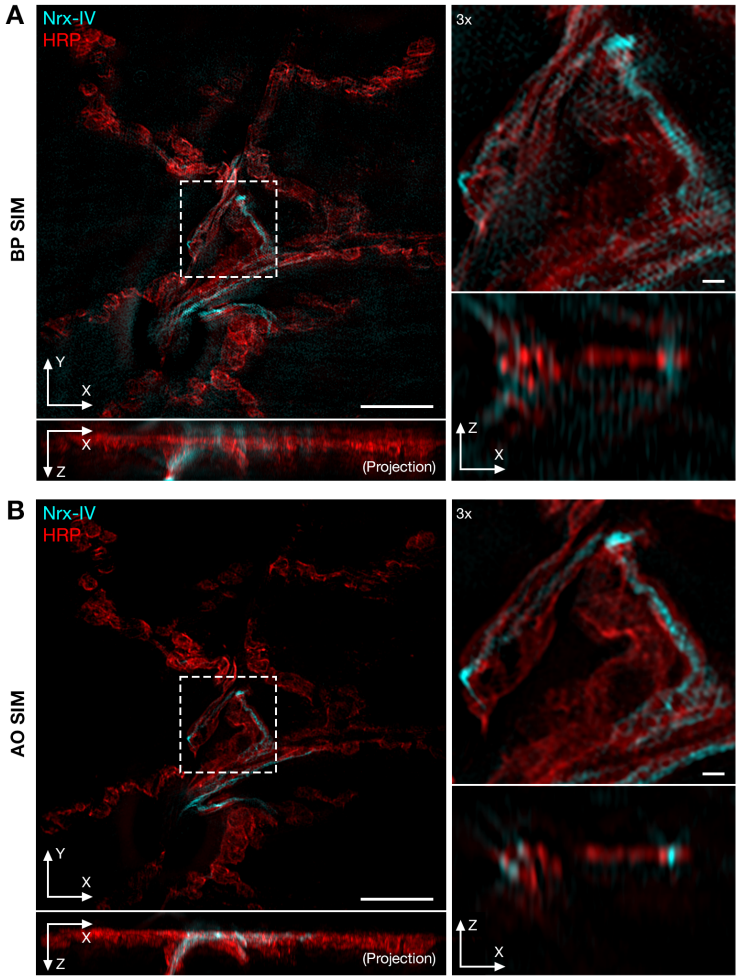

590

Figure 3. AO correction removes artefacts and improves the contrast and resolution of 3D-SIM in tissue imaging. (**A**, **B**) 3D-SIM images of neuromuscular junction in a fixed L3 *Drosophila* larva expressing Nrx-IV::GFP (cyan) and membrane labelled with anti-HRP
595 antibodies (red) acquired without (**A**) and with AO (**B**), respectively: top-left, maximum projection of the acquired volumes, scale bar is 10 μm; bottom-left, XZ view along Y drawn at the image centre; top-right, 3x zoom of the boxed area in XY view, scale bar is 1 μm; bottom right, XZ view of the zoomed area along Y at the image center.

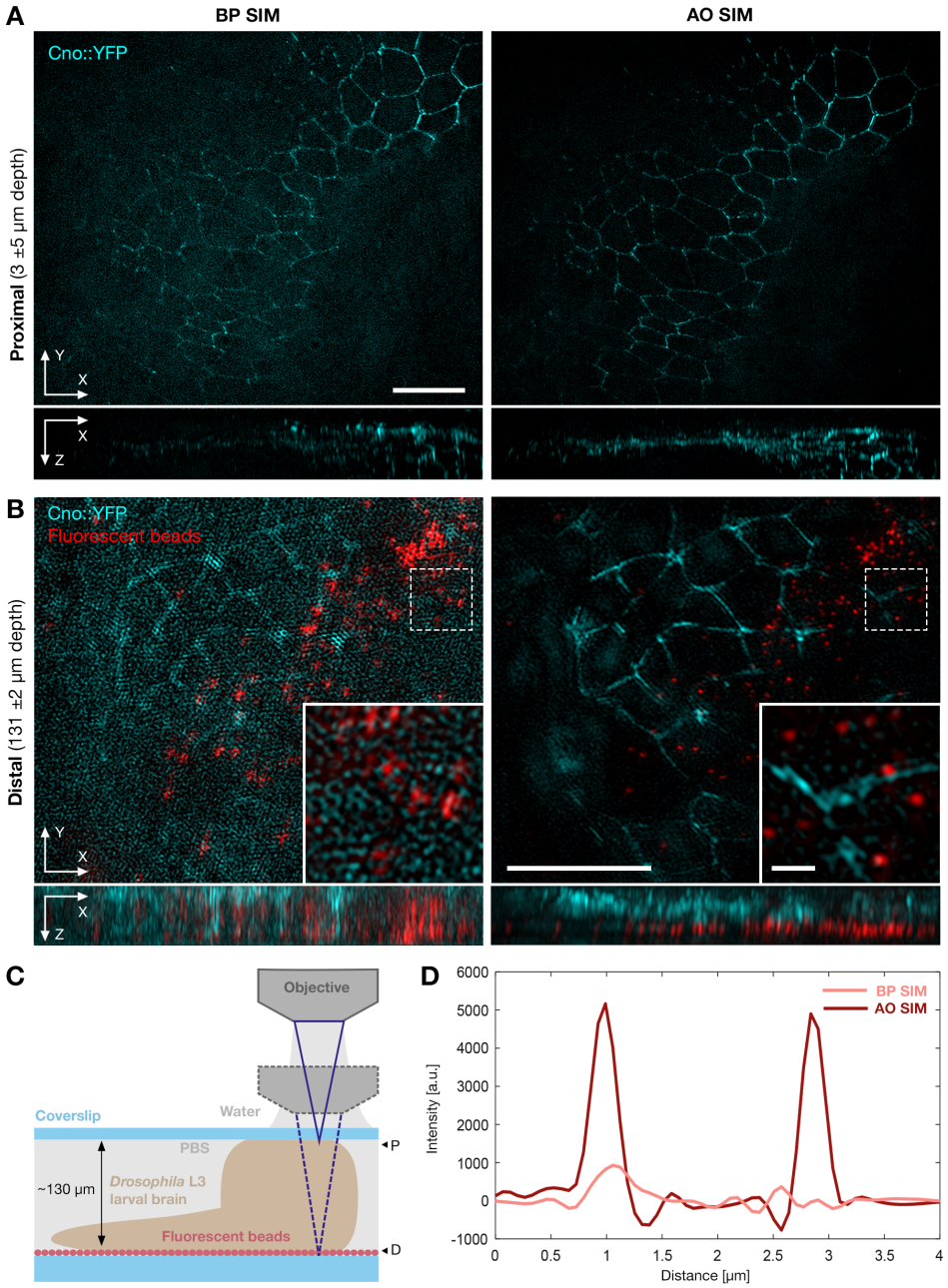

Figure 4. 3D-SIM in deep tissue samples enabled by AO aberrations correction. (**A**) 3D-SIM image stack of fixed *Drosophila* L3 larval brain imaged from top downwards at a depth of ~ 3 µm from the coverslip surface without AO (left) and with AO (right). Lateral view (XY; ~2 µm projection) and orthogonal views (XZ; projection of all slices). Expressed Cno::YFP (cyan) is located at the adherent junctions between neuroepithelial stem cells in the outer proliferation centers in the optic lobes. Scale bar: 10 µm. (**B**) 3D-SIM images of the same fixed *Drosophila* L3 larval brain, acquired through the entire volume of a single brain lobe at >130 µm from the top surface, with 100 nm diameter fluorescent beads attached to the surface of the glass slide (red). Images are displayed as in panel A but at 2-fold

610 magnification. Zoomed-in display of boxed areas showing that with AO correction, a resolution of ~200 nm is retained at depth, while the same information cannot be restored from the images acquired without AO. Scale bars: 10 μm and 1 μm (inset). (**C**) Schematic illustration of the specimen mounting and imaging. The larval brain was mounted in PBS between a glass coverslip (top) and a glass slide (bottom); the slide was coated with red
615 fluorescent beads at medium density. Image stacks in panels A and B were recorded at the proximal (arrowhead P) and distal side (arrowhead D) of the brain, respectively. (**D**) Example profile plots of two neighbouring beads highlighting the peak intensity improvement with AO correction.

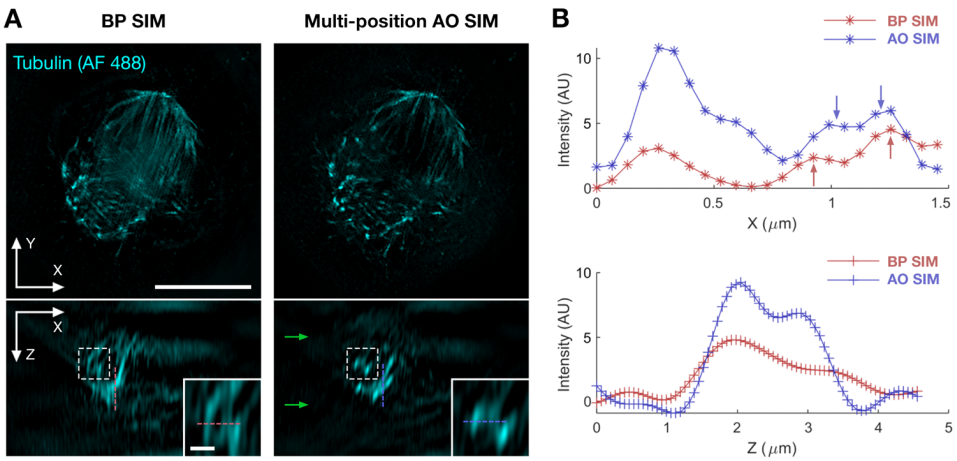

Figure 5. Multi-position aberration correction improves 3D-SIM resolution and contrast over a larger volume. (**A**) COS-7 cell in metaphase with microtubules immunostained with Alexa Fluor 488 visualizing the mitotic spindle. The volumes were acquired with remote focusing. Lateral (top) and orthogonal cross-section through a central area without (BP SIM, left) and with multi-position AO (right). Aberration measurements were performed at two imaging planes, one on the top and the other on the bottom of the cell volume (indicated by green arrows); dynamic correction was applied for all intermediate planes. Scale bar: 10 µm, and 1 µm (inset). (**B**) Plots of image pixel values along X and Z directions along the red and blue dashed lines in panel A show increased peak signal and resolution in the multi-position AO dataset.

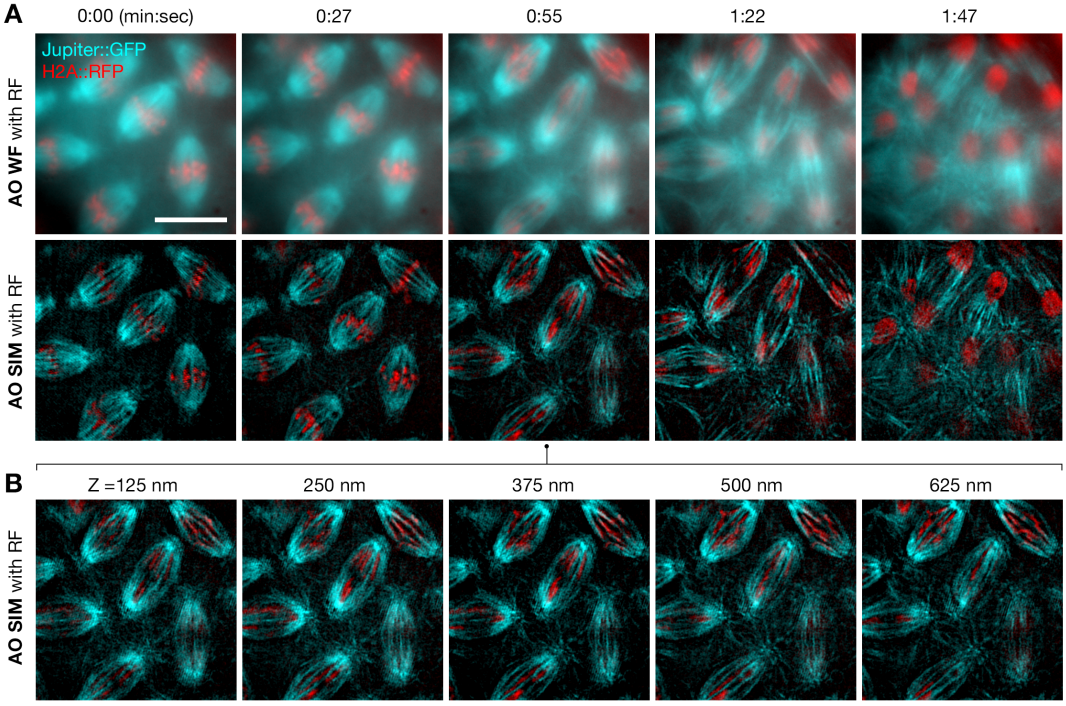

Figure 6. Remote focusing enables fast live 3D-SIM time-lapse imaging in *Drosophila* syncytial blastoderm embryos, without any mechanical actuation. The mitotic embryonic divisions are visualised by transgenic Jupiter::GFP expression to label microtubules (cyan) and transgenic Histone H2A::RFP expression to visualise chromosomes (red). (**A**) Mid-section of widefield and 3D-SIM reconstructions of the same 4D (3D+time) data, respectively. (**B**) Consecutive optical sections of the central time point (0:55) in panel A. Scale bar: 10 µm.

References

Antonello, J., J. Wang, C. He, M. Phillips, and M. Booth. 2020. Interferometric calibration of a deformable mirror. *Zenodo. 2020b doi*. 10.

Ball, G., J. Demmerle, R. Kaufmann, I. Davis, I.M. Dobbie, and L. Schermelleh. 2015. SIMcheck: a toolbox for successful super-resolution structured illumination microscopy. *Scientific reports*. 5:15915.

Bitenc, U., N.A. Bharmal, T.J. Morris, and R.M. Myers. 2014. Assessing the stability of an ALPAO deformable mirror for feed-forward operation. *Optics express*. 22:12438-12451.

Brent, J.R., K.M. Werner, and B.D. McCabe. 2009. Drosophila larval NMJ dissection. *JoVE (Journal of Visualized Experiments)*:e1107.

Corbett, A.D., M. Shaw, A. Yacoot, A. Jefferson, L. Schermelleh, T. Wilson, M. Booth, and P.S. Salter. 2018. Microscope calibration using laser written fluorescence. *Optics express*. 26:21887-21899.

Demmerle, J., C. Innocent, A.J. North, G. Ball, M. Müller, E. Miron, A. Matsuda, I.M. Dobbie, Y. Markaki, and L. Schermelleh. 2017. Strategic and practical guidelines for successful structured illumination microscopy. *Nature Protocols*. 12:988-1010.

Gao, L., L. Shao, C.D. Higgins, J.S. Poulton, M. Peifer, M.W. Davidson, X. Wu, B. Goldstein, and E. Betzig. 2012. Noninvasive imaging beyond the diffraction limit of 3D dynamics in thickly fluorescent specimens. *Cell*. 151:1370-1385.

Gustafsson, M.G., L. Shao, P.M. Carlton, C.J. Wang, I.N. Golubovskaya, W.Z. Cande, D.A. Agard, and J.W. Sedat. 2008. Three-dimensional resolution doubling in wide-field fluorescence microscopy by structured illumination. *Biophys J*. 94:4957-4970.

Hailstone, M., D. Waithe, T.J. Samuels, L. Yang, I. Costello, Y. Arava, E. Robertson, R.M. Parton, and I. Davis. 2020. CytoCensus, mapping cell identity and division in tissues and organs using machine learning. *Elife*. 9:e51085.

Hall, N. 2020. Chapter 3.2. 2 'Accessible adaptive optics and super-resolution microscopy to enable improved imaging'. Ph. D. thesis, University of Oxford.

Hall, N., J. Titlow, M.J. Booth, and I.M. Dobbie. 2020. Microscope-AOtools: a generalised adaptive optics implementation. *Optics Express*. 28:28987-29003.

Huang, B., M. Bates, and X. Zhuang. 2009. Super-resolution fluorescence microscopy. *Annual review of biochemistry*. 78:993-1016.

Kam, Z., P. Kner, D. Agard, and J.W. Sedat. 2007. Modelling the application of adaptive optics to wide-field microscope live imaging. *Journal of Microscopy*. 226:33-42.

Kner, P., Z. Kam, D. Agard, and J. Sedat. 2011. Adaptive optics in wide-field microscopy. Proc. SPIE 7931, MEMS Adaptive Optics V, 79310K.

Kounatidis, I., M.L. Stanifer, M.A. Phillips, P. Paul-Gilloteaux, X. Heiligenstein, H. Wang, C.A. Okolo, T.M. Fish, M.C. Spink, and D.I. Stuart. 2020. 3D correlative cryo-structured illumination fluorescence and soft X-ray microscopy elucidates reovirus intracellular release pathway. *Cell*. 182:515-530. e517.

Li, Q., M. Reinig, D. Kamiyama, B. Huang, X. Tao, A. Bardales, and J. Kubby. 2017. Woofer–tweeter adaptive optical structured illumination microscopy. *Photon. Res.* 5:329-334.

Lin, R., E.T. Kipreos, J. Zhu, C.H. Khang, and P. Kner. 2021. Subcellular three-dimensional imaging deep through multicellular thick samples by structured illumination microscopy and adaptive optics. *Nature Communications*. 12:3148.

Matsuda, A., L. Schermelleh, Y. Hirano, T. Haraguchi, and Y. Hiraoka. 2018. Accurate and fiducial-marker-free correction for three-dimensional chromatic shift in biological fluorescence microscopy. *Scientific Reports*. 8:7583.

Mertz, J., H. Paudel, and T.G. Bifano. 2015. Field of view advantage of conjugate adaptive optics in microscopy applications. *Applied Optics*. 54:3498-3506.

Ogushi, S., A. Rattani, J. Godwin, J. Metson, L. Schermelleh, and K. Nasmyth. 2021. Loss of sister kinetochore co-orientation and peri-centromeric cohesin protection after meiosis I depends on cleavage of centromeric REC8. *Developmental Cell*. 56:3100-3114. e3104.

Parton, R.M., A.M. Vallés, I.M. Dobbie, and I. Davis. 2010. Live cell imaging in Drosophila melanogaster. *Cold Spring Harbor Protocols*. 2010:pdb. top75.

Phillips, M.A., M. Harkiolaki, D.M.S. Pinto, R.M. Parton, A. Palanca, M. Garcia-Moreno, I. Kounatidis, J.W. Sedat, D.I. Stuart, and A. Castello. 2020. CryoSIM: super-resolution 3D structured illumination cryogenic fluorescence microscopy for correlated ultrastructural imaging. *Optica*. 7:802-812.

Phillips, M.A., D.M. Susano Pinto, N. Hall, J. Mateos-Langerak, R.M. Parton, J. Titlow, D.V. Stoychev, T. Parks, T. Susano Pinto, and J.W. Sedat. 2022. Microscope-Cockpit: Python-based bespoke microscopy for bio-medical science. *Wellcome Open Research*. 6:76.

Poland, S.P., A.J. Wright, and J.M. Girkin. 2008. Active focus locking in an optically sectioning microscope utilizing a deformable membrane mirror. *Opt. Lett.* 33:419-421.

Richter, V., M. Piper, M. Wagner, and H. Schneckenburger. 2019. Increasing resolution in live cell microscopy by structured illumination (SIM). *Applied Sciences*. 9:1188.

Sahl, S.J., S.W. Hell, and S. Jakobs. 2017. Fluorescence nanoscopy in cell biology. *Nature reviews Molecular cell biology*. 18:685-701.

Schermelleh, L., P.M. Carlton, S. Haase, L. Shao, L. Winoto, P. Kner, B. Burke, M.C. Cardoso, D.A. Agard, and M.G. Gustafsson. 2008. Subdiffraction multicolor imaging of

the nuclear periphery with 3D structured illumination microscopy. *science*. 320:1332-1336.

Schermelleh, L., A. Ferrand, T. Huser, C. Eggeling, M. Sauer, O. Biehlmaier, and G.P. Drummen. 2019. Super-resolution microscopy demystified. *Nature cell biology*. 21:72-84.

Schermelleh, L., R. Heintzmann, and H. Leonhardt. 2010. A guide to super-resolution fluorescence microscopy. *Journal of Cell Biology*. 190:165-175.

Schindelin, J., I. Arganda-Carreras, E. Frise, V. Kaynig, M. Longair, T. Pietzsch, S. Preibisch, C. Rueden, S. Saalfeld, and B. Schmid. 2012. Fiji: an open-source platform for biological-image analysis. *Nature methods*. 9:676-682.

Susano Pinto, D.M., M.A. Phillips, N. Hall, J. Mateos-Langerak, D. Stoychev, T. Susano Pinto, M.J. Booth, I. Davis, and I.M. Dobbie. 2021. Python-Microscope–a new open-source Python library for the control of microscopes. *Journal of Cell Science*. 134:jcs258955.

Temma, K., R. Oketani, T. Kubo, K. Bando, S. Maeda, K. Sugiura, T. Matsuda, R. Heintzmann, T. Kaminishi, and K. Fukuda. 2023. Selective plane activation structured illumination microscopy. *bioRxiv*:2023.2006. 2019.545558.

Thomas, B., A. Wolstenholme, S.N. Chaudhari, E.T. Kipreos, and P. Kner. 2015. Enhanced resolution through thick tissue with structured illumination and adaptive optics. *Journal of biomedical optics*. 20:026006-026006.

Turcotte, R., Y. Liang, M. Tanimoto, Q. Zhang, Z. Li, M. Koyama, E. Betzig, and N. Ji. 2019. Dynamic super-resolution structured illumination imaging in the living brain. *Proceedings of the National Academy of Sciences*. 116:9586-9591.

Wang, J., E.S. Allgeyer, G. Sirinakis, Y. Zhang, K. Hu, M.D. Lessard, Y. Li, R. Diekmann, M.A. Phillips, and I.M. Dobbie. 2021. Implementation of a 4Pi-SMS super-resolution microscope. *Nature protocols*. 16:677-727.

Wang, J., and Y. Zhang. 2021. Adaptive optics in super-resolution microscopy. *Biophysics Reports*. 7:267.

Wang, Y., Z. Yu, C.K. Cahoon, T. Parmely, N. Thomas, J.R. Unruh, B.D. Slaughter, and R.S. Hawley. 2018. Combined expansion microscopy with structured illumination microscopy for analyzing protein complexes. *Nature Protocols*. 13:1869-1895.

Žurauskas, M., O. Barnstedt, M. Frade-Rodriguez, S. Waddell, and M.J. Booth. 2017. Rapid adaptive remote focusing microscope for sensing of volumetric neural activity. *Biomedical optics express*. 8:4369-4379.

Žurauskas, M., I.M. Dobbie, R.M. Parton, M.A. Phillips, A. Göhler, I. Davis, and M.J. Booth. 2019. IsoSense: frequency enhanced sensorless adaptive optics through structured illumination. *Optica*. 6:370-379.